Journal Name

ARTICLE

Hybrid Chemical Vapor Deposition Enables Scalable and Stable Cs-FA Mixed Cation Perovskite Solar Modules with a Designated Area of 91.8 cm^2 Approaching 10% Efficiency

Received 00th January 20xx,
Accepted 00th January 20xx

DOI: 10.1039/x0xx00000x

www.rsc.org/

Longbin Qiu,[†a] Sisi He,[†a] Yan Jiang,[a] Dae-Yong Son,[a] Luis K. Ono,[a] Zonghao Liu,[a] Taehoon Kim,[a] Theodoros Bouloumis,[a] Said Kazaoui,[b] Yabing Qi*[a]

The development of scalable deposition methods for stable perovskite layer is a prerequisite for the development and the future commercialization of perovskite solar modules. However, scalability and stability are the two main challenges to overcome towards the realization of perovskite solar modules. In sharp contrast to previous report, here we develop a fully vapor based scalable hybrid chemical vapor deposition (HCVD) process for depositing Cs- formamidinium (FA) mixed cation perovskite films, which alleviate the problem encountered using conventional solution coating of mainly methylammonium lead iodide ($MAPbI_3$). Using our HCVD technique, we fabricate perovskite films of $Cs_{0.1}FA_{0.9}PbI_{2.9}Br_{0.1}$ with enhanced thermal and phase stabilities, by the intimate incorporation of Cs into FA based perovskite films. In addition, the sputtered SnO_2 electron transport layer (ETL) is found to be damaged during the HCVD process. In combination with precise interface engineering of SnO_2 ETL, we demonstrate relatively large area solar modules with efficiency approaching 10% with a designated area of 91.8 cm^2 fabricated on 10 cm × 10 cm substrates (14 cells in series). On the basis of our preliminary operational stability tests on encapsulated perovskite solar modules, we extrapolated that the T_{80} lifetime is approximately 500 h (at 1 sun, 25 °C).

Introduction

The development of perovskite solar cells/modules remains unprecedented with the certified stabilized output efficiency of 20.9% for small cells (0.991 cm^2), 17.25% for mini-modules (17.277 cm^2) and 11.7% for submodules (703 cm^2).[1] However, there are still two main challenges to be addressed, namely scalability and stability, towards their potential commercialization.[2] As learned from other photovoltaic technologies (Si, CdTe), the absolute efficiency decay with upscaling the area is estimated to be approximately 0.8%/decade.[3] Hence, when a 1 cm^2 solar cell with 20% efficiency is upscaled to a solar module of 100 cm^2 designated area, the efficiency is expected to be 18.4%, according to the estimated decay rate. However, at the current stage the published results in the literature indicate that for perovskite solar cell devices the efficiency decays faster upon upscaling with the area.[3]

This can be explained mainly by two causes. Firstly, the decay in the efficiency would be related to perovskite deposition methods. By far the most efficient perovskite solar cells are processed by the spin-coating method and reported on small active areas, e.g., 0.1 cm^2 to 1 cm^2. A high quality perovskite film is easily obtained on this area.[4] However, film quality deteriorates as the film size increases to a typical module size, i.e., 100 cm^2.[2, 3] It is thus necessary to develop perovskite deposition methods capable of depositing large area films with high quality.[5] Currently, scalable solution coating methods including spray coating, slot-die coating and doctor blading are in rapid development. Large area methylammonium lead iodide ($MAPbI_3$) modules up to 45 cm × 65 cm have been demonstrated in a previous study.[6] However, this coating method is less efficient than that of the spin coating in small cells. Furthermore, the volatile solvents are not environmentally friendly. Beside solution coating methods, efforts have been made in utilizing vapor deposition for perovskite solar cells/modules, as it benefits from the conformal coating over large area, elimination of toxic solvents, precise film thickness control, and outstanding compatibility with tandem solar cell fabrication.[7] For example, the hybrid chemical vapor deposition (HCVD) process was developed to fabricate $MAPbI_3$ and formamidinium lead iodide ($FAPbI_3$) based solar modules.[8] In this process, perovskite films are formed in two steps. In the first step, a lead halide film such as PbI_2, $PbCl_2$ or $PbBr_2$ is deposited by thermal evaporation. In the second step, the as prepared lead halide film is reacted with

[a] Energy Materials and Surface Sciences Unit (EMSSU), Okinawa Institute of Science and Technology Graduate University (OIST), 1919-1 Tancha, Kunigami-gun, Onna-son, Okinawa 904-0495, Japan.
*Corresponding author: Yabing Qi, E-mail: Yabing.Qi@OIST.jp.
[b] Research Center for Photovoltaics (RCPV), National Institute of Advanced Industrial Science and Technology (AIST), Tsukuba, Ibaraki 305-8565, Japan.
† L. Qiu and S. He contributed equally to this work.
Electronic Supplementary Information (ESI) available.

organic halide species with controlled vapor atmosphere and pressure to form perovskite films inside a tube furnace. The composition of perovskite can be readily tuned by changing the organic vapor atmosphere, from MAI to FAI or MABr, to obtain $MAPbI_3$, $FAPbI_3$ or $MAPbBr_3$, respectively.[9] With the controllable deposition of perovskite, HCVD is promising for large scale fabrication of high performance/stable perovskite solar cells and light emitting diodes.[9] Secondly, the rapid decay in the efficiency can be also originated from the nonoptimal module design (non-ohmic interconnection contact between FTO/Au leading to high series resistance, large dead area due to P1, P2, P3 pattering). A likely cause responsible for the faster efficiency decay upon upscaling area comes from the transparent conducting electrode sheet resistance, which often leads to reduction in the fill factor.[10] The module design of stripes in series connection is a solution that can significantly increase the aspect ratio of each sub-cell and reduce the resistance effect. The maximum stripe width is limited by the transparent conducting electrode sheet resistance.[11] In this design, the relation between the stripe width and the transparent conducting electrode sheet resistance should be considered, as for each stripe there will be an area for making interconnection, which is a dead area. To get lower resistance a narrower stripe is required, and the active area to the total area ratio (geometric fill factor, GFF) is also lower. In addition, using mask-patterning instead of other fine controlled patterning techniques such as laser scribing or mechanical scribing results in the GFF as low as 50%, at the early stage of the perovskite solar module design.[8, 12] On the basis of the calculation result, for highly conductive FTO substrates (10 Ω/□), the stripe width could be up to 7 mm with a small dead area to reach the maximum power output.[10] GFF as high as 95% has been demonstrated by using the laser patterning technique and this offers a better design for active area approaching the total area of the substrate.[13]

Another aspect to be considered is the operational lifetime. Although number of reports on the perovskite solar modules is increased gradually, they are mainly based on solution coated $MAPbI_3$.[2] With modified precursor solution properties by adding surfactant, large area 57.2 cm^2 solar modules with doctor blading $MAPbI_3$ have been fabricated with an efficiency up to 14.6%.[14] In another work, by adding excess MACl into the $MAPbI_3$ precursor ink, high quality film has been deposited by blade coating and module with 12.6 cm^2 showed efficiency of 13.3%.[15] The efficiency was further improved to 15.6% with $MA_{0.7}FA_{0.3}PbI_3$ and interconnection optimization.[16] From an intermediate design of PbI_2·nMA and MAI·mMA precursor, solvent- and vacuum-free tape assisted coating process has been developed for $MAPbI_3$ based modules, with a certified efficiency of 12.1% on an area of 36.1 cm^2.[5] The slot-die coated perovskite solar module with an area up to168.75 cm^2 was also based on $MAPbI_3$, with the efficiency reaching 10%.[17] Although the area and efficiency are increasing with research efforts, $MAPbI_3$ is not suitable for commercialization, due to its instability under heat, light, humidity and oxygen.[18] A new trend in the field is to employ thermally more stable FA based mixed cation (especially Cs cation) perovskites to improve stability.[19] In FA based mixed cation perovskite, a small amount of Cs could stabilize the perovskite phase for high performance and stability.[20] In addition, with the Cs concentration in the range of 10-30%, charge-carrier mobility, charge-carrier lifetime and crystal quality are substantially improved.[21] A few works reported the solution coating of Cs containing FA based perovskite solar cells, however, very few studies reported solar modules.[2, 22] Our group previously reported the successful fabrication of mini-modules with $Cs_{0.07}FA_{0.93}PbI_3$ based perovskite utilizing cation exchange process.[23] These mini-modules showed high stability under continues light illumination. A recent report during the preparation of this work is related to $Cs_xFA_{1-x}PbI_{3-y}Br_y$ based perovskite solar modules fabricated using vapor-solid reaction method that could be considered as a combination of physical vapor deposition and low pressure chemical vapor deposition.[24] We would like to stress that these reported modules are characterized by a relatively modest GFF, and relative small active areas (12 cm^2 on a 5 cm × 5 cm substrate, with 6 cells in series[23] and 41.25 cm^2 on an 8 cm × 8 cm substrate, with 9 cells in series[24]). To further scale up FA based mixed cation perovskites with large area and also high GFF is important for the development of perovskite solar modules.

Here we show the scalability of the HCVD process in deposition of FA-Cs based mixed perovskites for large area stable solar modules on10 cm × 10 cm substrates with a high GFF (90%). This fully vapor based process eliminates the use of toxic solvents such as dimethylformamide and dimethyl sulfoxide, which are not environmentally friendly. The composition of the perovskite layer could be readily changed from $MAPbI_3$ to $FAPbI_3$ and FA-Cs mixed cation perovskite, by controlling the precursor composition during HCVD process. With co-evaporation of CsBr and PbI_2 in the first step, followed by exposure to FAI vapor in the second step, we successfully fabricated Cs-FA perovskite such as $Cs_{0.1}FA_{0.9}PbI_{2.9}Br_{0.1}$ through a fully vapor based process. We also find that one critical issue for HCVD perovskite solar cells/modules is the vacuum annealing process which might damage the SnO_2 layer. A C_{60} layer with a thickness of 5 nm was inserted between SnO_2 and perovskite, which passivate and modulate the energy levels at these interfaces. Benefiting from the fully vapor deposition HCVD process, the film and interface showed little difference between small area cells and large area modules. With the area increasing by 1000-fold from 0.09 cm^2 to 91.8 cm^2, we demonstrate that the device designated area PCE decreases slightly (from 13.3% to 9.34%, which corresponds to a PCE drop of 1.3%/decade), suggesting that this fully vacuum deposition process is a promising route towards scalability. In addition, the HCVD method is promising because it allows the synthesis of relatively stable perovskite composition such as $Cs_{0.1}FA_{0.9}PbI_{2.9}Br_{0.1}$. The operational lifetime of these encapsulated Glass/FTO/SnO_2/C_{60}/perovskite/spiro-MeOTAD/Au/parylene/Glass solar modules has been studied, and showed

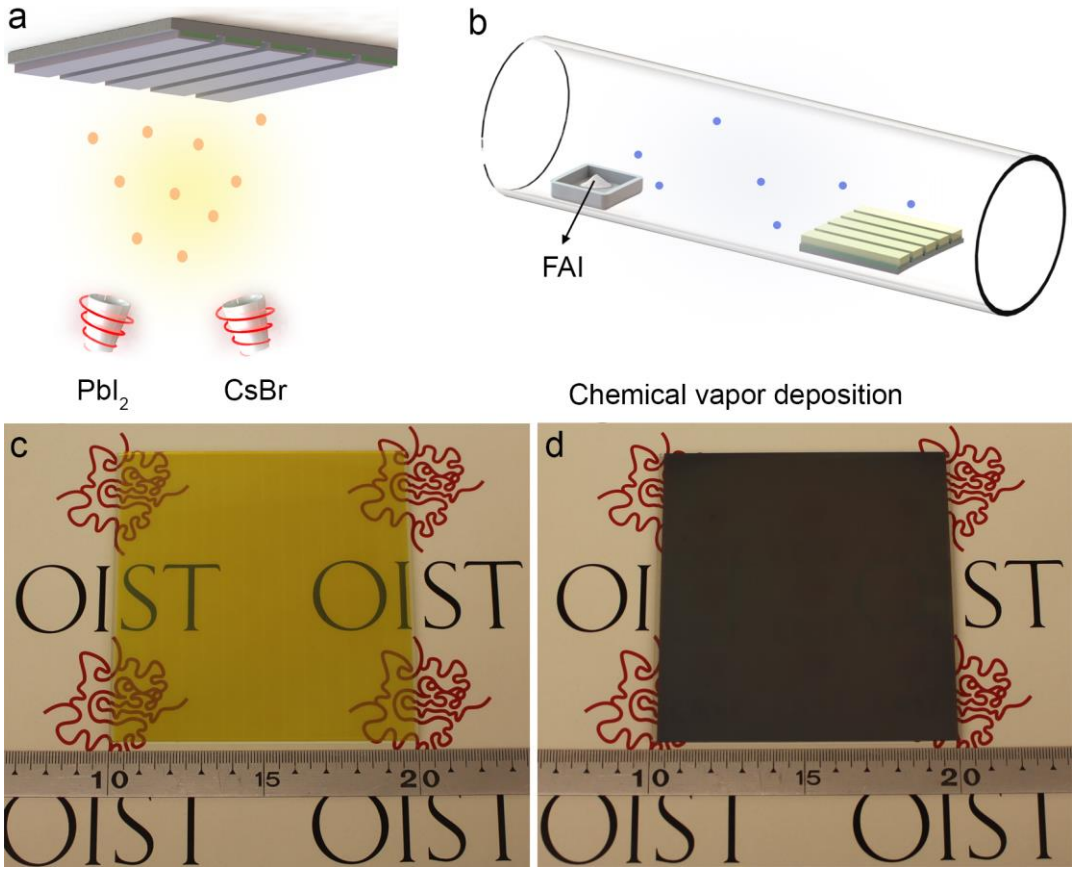

Figure 1. Schematic drawing showing the HCVD process. a) Thermal evaporation of inorganic precursors including PbI_2 and CsBr. **b)** HCVD of FAI organic precursor for the formation of perovskite. Optical image of **c)** co-evaporated PbI_2/CsBr film and **d)** HCVD $Cs_{0.1}FA_{0.9}PbI_{2.9}Br_{0.1}$ perovskite film (96 cm^2 on the 100 cm^2 patterned FTO substrate).

an extrapolated T_{80} lifetime of approximately 500 h under one sun continuous illumination and steady state power output.

Results and discussion

Hybrid Chemical Vapor Deposition

Figure 1 displays the fully vapor based HCVD process for the fabrication of perovskite films with controlled compositions. The perovskite formation proceeds into two steps as we previously developed.[9] The first step (Figure 1a) is slightly modified, with the vacuum co-evaporation of inorganic precursors including PbI_2 and CsBr. The intended composition in this work is 10% Cs and 90% FA cation, considering a suitable band-gap for single junction solar cells, phase stability, and high quality.[21] A small amount of Br is incorporated to further improve the perovskite stability.[25] Although a layer-by-layer deposition of CsBr and PbI_2 might help precisely control the thickness of each layer,[26] after the HCVD process, the resulted film will have a gradient composition structure because the interdiffusion of CsBr and PbI_2 (both are much less volatile than FAI) during the HCVD process is expected to be much slower than FAI. Based on such consideration, we employed co-evaporation on this work to ensure uniform distribution of the CsBr - PbI_2 mixed film. To achieve 10% Cs, the evaporation rate of PbI_2 and CsBr are controlled to be 0.10 nm/s and 0.01 nm/s, respectively. The deposition rate and thickness of the co-evaporated film are monitored by quartz crystal microbalance (QCM). The thickness of the co-evaporated PbI_2/CsBr film is approximately 185 nm. In the second step (Figure 1b), the PbI_2/CsBr coated substrate is transferred into a multi-zone tube furnace with the FAI organic precursor in the upstream side and the substrates are placed in the downstream side. Upon exposure to FAI vapor and at 150 °C, PbI_2/CsBr film readily converts into $Cs_{0.1}FA_{0.9}PbI_{2.9}Br_{0.1}$ perovskite films. As shown in Figure 1c and d, the yellow co-evaporated PbI_2/CsBr film and a dark brown $Cs_{0.1}FA_{0.9}PbI_{2.9}Br_{0.1}$ perovskite film are uniformly coated on the stripe-patterned FTO substrate, with a size of 10 cm × 10 cm. These results demonstrate the excellent apparent uniformity of the as-prepared $Cs_{0.1}FA_{0.9}PbI_{2.9}Br_{0.1}$ perovskite film.

The microstructure of the co-evaporated PbI_2/CsBr film and $Cs_{0.1}FA_{0.9}PbI_{2.9}Br_{0.1}$ perovskite film after HCVD is further studied (Figure 2). The cross-section image of co-evaporated PbI_2/CsBr film on top of FTO confirms that the PbI_2/CsBr film consists of nano-plates with large roughness (Figure 2a and c). The thickness of this PbI_2/CsBr layer is expected to be 185 nm, monitored by QCM during the thermal evaporation. However, due to the rough surface as shown in Figure 2a, it is difficult to determine the thickness accurately. After the HCVD process with the FAI vapor, the perovskite film thickness is approximately 400 nm (Figure 2b), and is characterized by large grains and ultra-smooth surface (Figure 2d). The film thickness

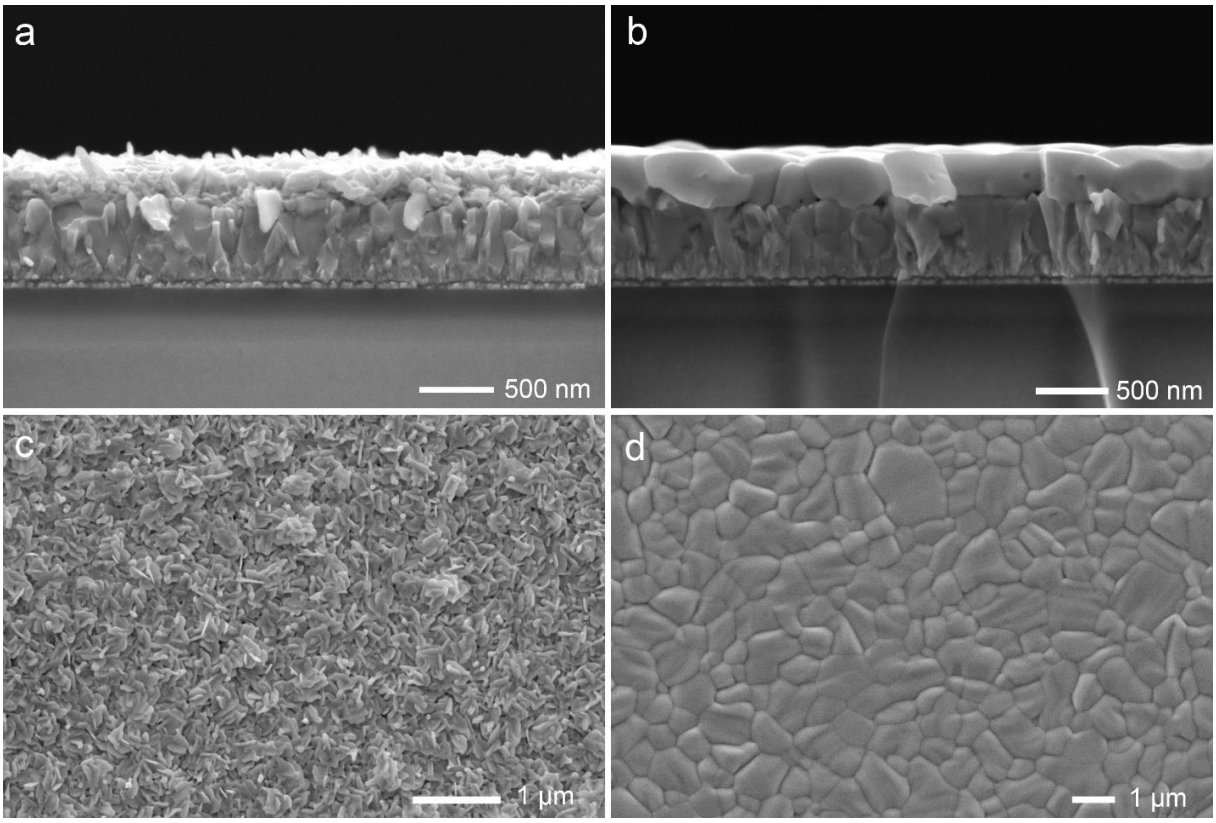

Figure 2. Microstructure of PbI_2/CsBr before and after HCVD. Cross-section SEM image of **a)** PbI_2/CsBr and **b)** $Cs_{0.1}FA_{0.9}PbI_{2.9}Br_{0.1}$ perovskite films. Surface SEM image of **c)** PbI_2/CsBr and **d)** $Cs_{0.1}FA_{0.9}PbI_{2.9}Br_{0.1}$ perovskite films.

after the HCVD is found to increase by a factor of 2.16. The thickness increase of the fully converted perovskite film could be estimated from the density of PbI_2 (6.16 g/cm^3) and $FAPbI_3$ (4.10 g/cm^3).[9b, 27] With the assumption of full conversion and exclusion of the small amount of Cs, the expected thickness would increase by a factor of 2.03, which is in good agreement with the cross-section SEM images (Figure 2d). These results confirm the excellent uniformity of the as-prepared $Cs_{0.1}FA_{0.9}PbI_{2.9}Br_{0.1}$ perovskite film.

The crystal structure and composition of the HCVD deposited $Cs_{0.1}FA_{0.9}PbI_{2.9}Br_{0.1}$ perovskite film have been further characterized. From Figure 3a the (110) perovskite peak at 13.99° is clearly observed without any residual PbI_2 signal at 12.6° after HCVD (inset in Figure 3a), which confirms that FAI could diffuse into the bottom and completely react with PbI_2/CsBr film. Furthermore, no diffraction peaks appear at 11.7° corresponding to the non-perovskite phase of $FAPbI_3$, suggesting the good phase purity of the $Cs_{0.1}FA_{0.9}PbI_{2.9}Br_{0.1}$ perovskite films prepared by HCVD. The optical absorbance edge of the perovskite film is 798 nm (Figure 3b), which corresponds to an optical band of 1.56 eV from Tauc-plot (Figure S1). To study the composition of the perovskite film, X-ray photoelectron spectroscopy (XPS) is performed (Table S1). Before and after HCVD the ratio between Cs and Pb is approximately 0.1, which is consistent with deposition rate monitored by QCM (Figure 3c and d). After HCVD, the core level of Br 3d is weaker (Figure 3e).[28] Regarding the decreased Br 3d signal, whether this is because there is phase separation on the top surface or the Br actually evaporates after HCVD process is currently under further investigation. The XPS mapping further confirms the uniform distribution of Cs and Br in the perovskite layer (Figure S2). To confirm the composition, $Cs_{0.1}FA_{0.9}PbI_{2.9}Br_{0.1}$ film made by solution coating process has been prepared and compared with $Cs_{0.1}FA_{0.9}PbI_{2.9}Br_{0.1}$ made by HCVD.[25] As shown in Figure S3-4, the XRD and UV-vis absorbance of $Cs_{0.1}FA_{0.9}PbI_{2.9}Br_{0.1}$ synthesized by solution and HCVD methods are very similar and thus we infere that their composition are also similar. The reaction of PbI_2/CsBr with FAI and annealing at ~150 °C seems to relatively decrease the concentration of Br on the top surface of perovskite (Figure S5). The core level of N 1s is ascribed to FA cation, which also indicates the incorporation of FAI for the perovskite formation (Figure 3f).

Small area solar cells

The carrier lifetime of $Cs_{0.1}FA_{0.9}PbI_{2.9}Br_{0.1}$ on bare glass made by HCVD was investigated by time-resolved photoluminescence (TRPL), as presented in Figure S6. The upper limit of the open-circuit voltage (V_{OC}) due to the non-radiative recombination in the perovskite is calculated to be approximately 1.04 V at room temperature (Supporting Note 1).[11, 29] Further study are necessary to improve the film quality and to reduce the defects density to achieve long carrier lifetime.[30] To check the photovoltaic performance of this HCVD deposited $Cs_{0.1}FA_{0.9}PbI_{2.9}Br_{0.1}$ film, a planar junction structured device has been applied with sputtered SnO_2 as electron transport layer (ETL) (Figure 4a). The sputtered SnO_2 film has been optimized according to our recent work and achieves an efficiency over 20% based on spin coated perovskite films.[31] However, the

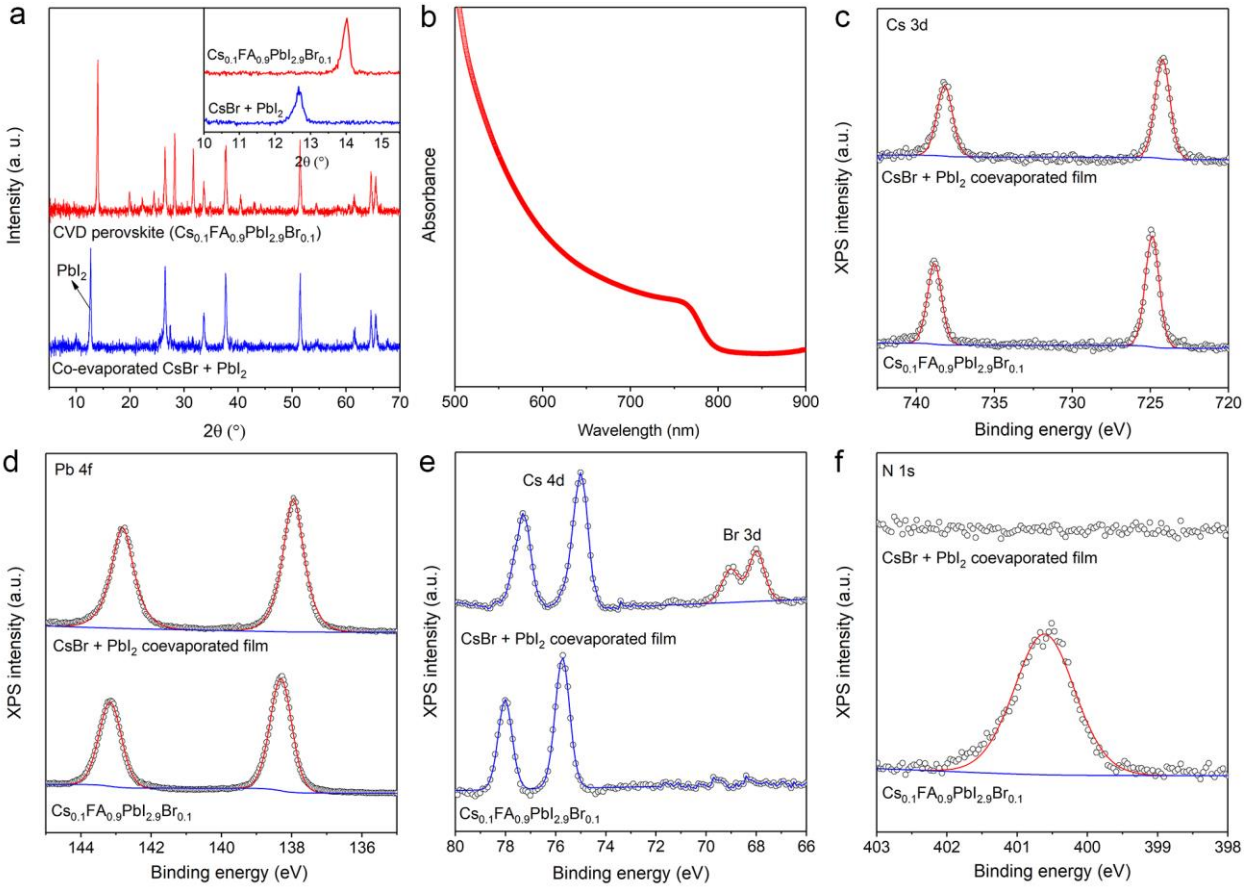

Figure 3. Structure and composition of HCVD perovskite layer. a) XRD before and after HCVD, which indicate high quality perovskite structure. **b)** Optical absorbance of $Cs_{0.1}FA_{0.9}PbI_{2.9}Br_{0.1}$. Core level of **c)** Cs 3d, **d)** Pb 4f, **e)** Br 3d and **f)** N 1s before and after HCVD, which indicate the formation of $Cs_{0.1}FA_{0.9}PbI_{2.9}Br_{0.1}$.

HCVD device performance is lower than expected. As shown in Figure S7, from the typical J-V curves of the solar cells, the V_{OC} is average only 0.81 V (Table S2), which is much lower than the calculated upper limit due to the non-radiative recombination (1.04 V). We find that the vacuum annealing process during HCVD damages the SnO_2 layer. Ultraviolet photoemission spectroscopy (UPS) and XPS measurements of the SnO_2 layer before and after vacuum annealing process have been performed to study the gap states (Figure S8). These states are believed to be mainly caused by oxygen deficiency after vacuum annealing (Figure S9). These gap states after the vacuum annealing process lower the hole-blocking properties of the SnO_2 ETL.[31, 32] To confirm the effect of the vacuum annealing process, a control experiment has been performed. Solution processed devices were fabricated on sputtered SnO_2 with and without vacuum annealing process. As shown in Table S3 and Figure S10, the photovoltaic performance of solution coated perovskite solar cells on sputtered SnO_2 with and without vacuum annealing process differ significantly. After vacuum annealing the SnO_2 performance degrades significantly, and all the device photovoltaic parameters decrease. Especially the V_{OC} decreases from 1.03 V to 0.73 V. As a control experiment the vacuum annealing effect has also been studied based on mostly used SnO_2 film prepared from Alfa Aesar solution.[33] This crystalline SnO_2 film also shows reduced performance after vacuum annealing process (Table S3). It shows that the negative effect induced by vacuum annealing is not limited to sputtered SnO_2 films. Note that this is not unique to SnO_2, because it also occurs for TiO_2 annealed in inert atmosphere (such as in N_2 glove box) where oxygen defect deteriorate the perovskite solar cells performance.[34]

In this case, SnO_2 surface modification is necessary to achieve high quality for electron extraction and hole blocking. A thin layer of C_{60} has been evaporated on top of SnO_2 before co-evaporation of PbI_2/CsBr as a buffer and passivation layer. The energy level diagram from UPS measurement is shown in Figure S11, which confirms the smooth transfer of charges crossing the interface.[35] Regarding the influence on the SnO_2 films induced by vacuum annealing, we further performed a control experiment on a sputtered SnO_2/C_{60} electron transport layer before and after vacuum annealing to study the effect of C_{60} passivation (Table S3). Note that in the case of "SnO_2/C_{60}", the efficiency with vacuum annealing is only slightly lower than that without vacuum annealing, suggesting that the negative effect of vacuum annealing is largely mitigated by adding a thin film of C_{60} with a thickness of 5 nm. However, when comparing the case of SnO_2/C_{60} with the case of SnO_2 before vacuum annealing, the device efficiency is about 10-20% lower in the case of SnO_2/C_{60}. The factor that might influence the device performance in the case of SnO_2/C_{60} is air exposure during the sample transfer. It has been shown that C_{60} has poor air stability, which may induce oxygen-trap states and decrease charge carrier lifetime.[36] Air exposure after C_{60} deposition is proposed to be the main reason for the lower performance. With this vacuum deposited SnO_2/C_{60} bilayer as ETL, solar cells based on perovskite $Cs_{0.1}FA_{0.9}PbI_{2.9}Br_{0.1}$ made by HCVD have

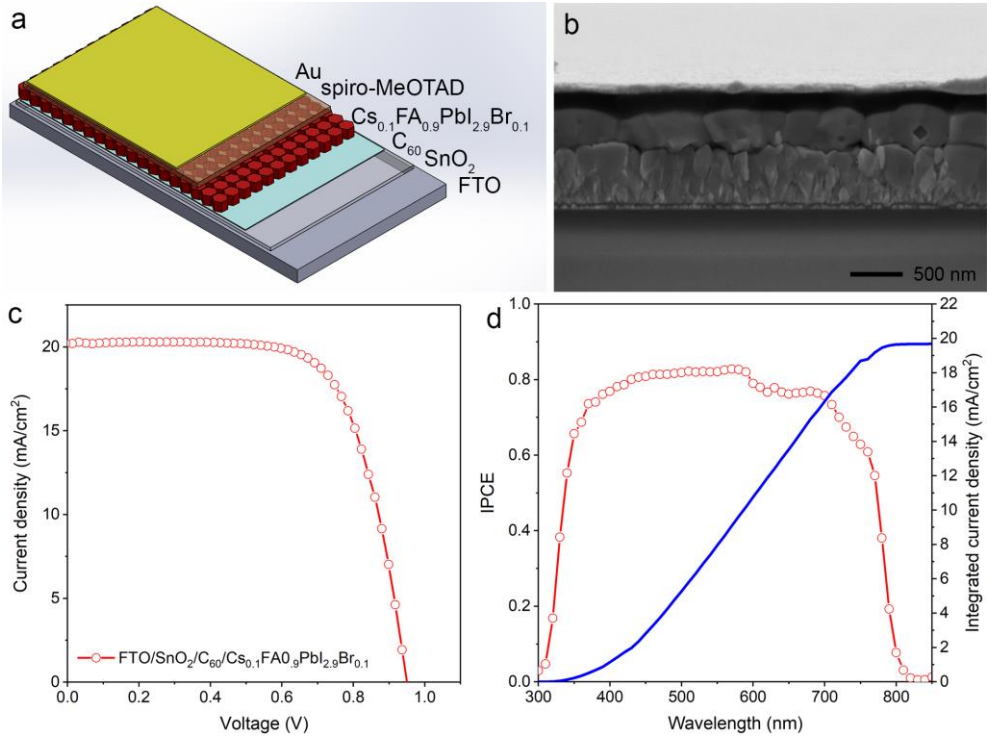

Figure 4. $Cs_{0.1}FA_{0.9}PbI_{2.9}Br_{0.1}$ based planar junction solar cell performance. a) Schematic drawing showing the planar junction device structure. b) Cross-section SEM image of the HCVD $Cs_{0.1}FA_{0.9}PbI_{2.9}Br_{0.1}$ based solar cell. Typical c) J-V curve and d) IPCE spectra of HCVD $Cs_{0.1}FA_{0.9}PbI_{2.9}Br_{0.1}$ based solar cells.

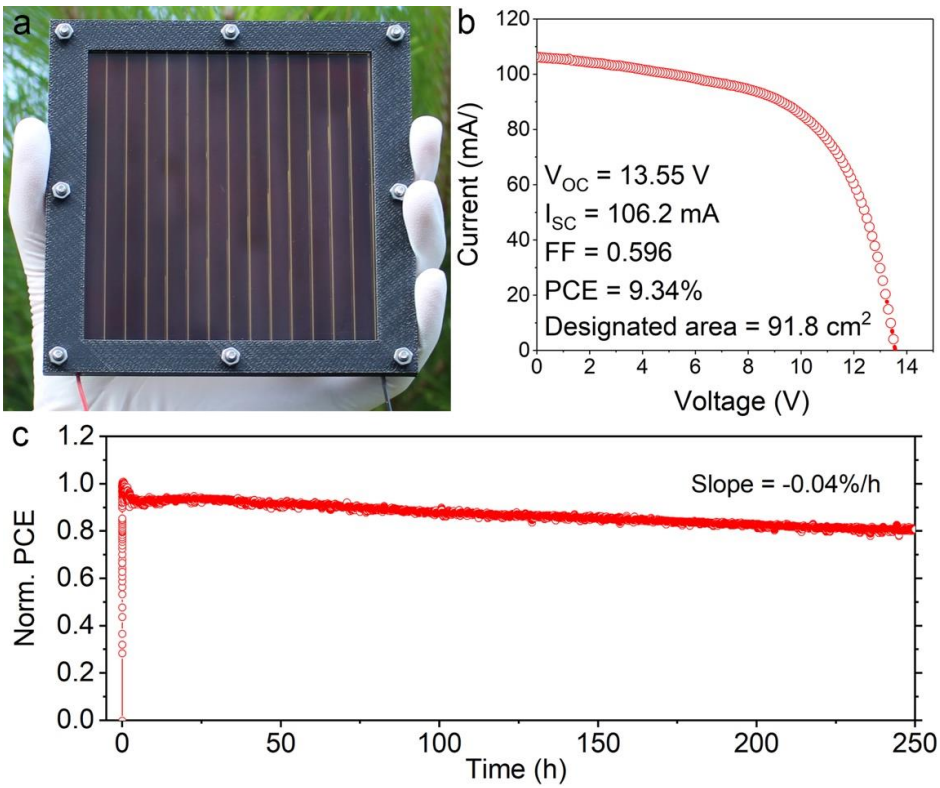

Figure 5. $Cs_{0.1}FA_{0.9}PbI_{2.9}Br_{0.1}$ based solar module performance. a) Optical image of a 10 cm × 10 cm HCVD $Cs_{0.1}FA_{0.9}PbI_{2.9}Br_{0.1}$ based solar module. b) J-V curve of the champion 10 cm × 10 cm HCVD $Cs_{0.1}FA_{0.9}PbI_{2.9}Br_{0.1}$ based solar module (14 sub-cells in series). c) Operational stability of HCVD solar module under one-sun illumination and steady-state power output tracking.

been fabricated with the structure Glass/FTO/SnO_2/C_{60}/Perovskite/spiro-MeOTAD/Au (Figure 4a). A clear layer by layer structure of the planar junction device can be observed in the cross-section SEM image (Figure 4b). The active layer thickness is around 400 nm. With this planar junction structure the champion small cell efficiency is 13.3%

(0.09 cm^2). Improving the perovskite optoelectronic quality and engineering the perovskite and ETL interfaces to reducing the non-radiative carrier recombination rates at bulk and interfaces are possible strategies to further push up the solar cell performance. As shown in Figure 4c, from the typical J-V curve of solar cells with HCVD $Cs_{0.1}FA_{0.9}PbI_{2.9}Br_{0.1}$, the V_{OC} is on average 0.90 V (Table S2). The short circuit current density (J_{SC}) is around 20.2 mA/cm^2, which is consistent with IPCE spectra (Figure 4d). Currently, the average fill factor is around 0.67 leaving room for further improvement.

Large area solar modules

The deposition process is very promising for large scale solar module fabrication. The scale-up of the $Cs_{0.1}FA_{0.9}PbI_{2.9}Br_{0.1}$ solar cells to 10 cm × 10 cm solar modules through the HCVD method is further demonstrated (Figure 5a). The module comprises 14 sub-cells in series connection. For each FTO stripe, the width is 6.6 mm, with 0.1 mm P1 pattering in between each FTO stripe. The length of the stripe is 98 mm results in the area of 6.468 cm^2 for each stripe. The interconnection area is formed by CO_2 laser scribing, with a width around 0.15 mm (P2). Finally, mechanical scribing is used to separate each sub-cell by forming a P3 patterning (0.05 mm). The P1-P2-P3 patterning is shown in Figure S12. Considering the FTO stripe width plus P1 width (6.7 mm) and the dead area for sub-cell series connection (0.68 mm), the geometric fill factor is up to 90%. 10 solar modules have been fabricated, the photovoltaic parameters of which are listed in Table S4. The champion solar module is plotted in Figure 5b. The modules have been further encapsulated by deposition of a Parylene film[37] on top of Au electrode side and then a cover glass is sealed on top with UV-curable glue on the edges to further prevent water and oxygen infiltration as well as to ensure a good thermal contact with cooling stage to dissipate heat (Figure S13). This low temperature encapsulation process does not affect the module performance (Figure S14). The best performance is 9.34% with a designated area of 91.8 cm^2 (Figure 5b) and the active area efficiency reaches 10.37% (active area = 82.6 cm^2).

With a GFF of 90%, the short-circuit current (I_{SC}) is expected to be 119 mA considering the J_{SC} value obtained from the small cell (20.2 mA/cm^2) and the area of each cell stripe (5.909 cm^2). Indeed, the measured I_{SC} from solar modules is mostly around 110 mA (Table S4), which clearly demonstrates the fine pattering process and the scalability of our HCVD method. The average V_{OC} for modules is 12.8 V and for each sub-cell is 0.91 V. The V_{OC} of sub-cells in the modules also matches well the value obtained for the small area cells (Table S2 and S4). From the small area cells to modules, the area is enlarged by over 1000 time (from 0.09 cm^2 to 91.8 cm^2). The champion efficiency decreased from 13.3% to 9.3% (active area efficiency 10.4%) (Figure S15), which is only slightly lower than expectation (10.9%) if assuming an efficiency-against-area decay rate of 0.8%/decade. The decrease mainly comes from the lower fill factor. Without removing bottom SnO_2 (17 nm), the contact resistance might also increase compared with Au/FTO interface contact resistance, which might be the main cause for the lower fill factor.[38] This module shows hysteresis with a hysteresis factor around 0.17 (hysteresis factor = ($PCE_{Reverse}$ – $PCE_{Forward}$)/$PCE_{Reverse}$) (Figure S16),[39] which need further engineering of interface and perovskite composition.[33, 39] As a demonstration of the broad composition adjustment of perovskite by HCVD, the same 10 cm × 10 cm size modules but with $MAPbI_3$ active layer have been fabricated. The performance is lower than that of the $Cs_{0.1}FA_{0.9}PbI_{2.9}Br_{0.1}$ based solar modules (Figure S17), due to the mismatch of the energy level alignment as shown in Figure S11. This demonstrates the scalability of our HCVD method for large area monolithic perovskite solar modules, with desired composition.

The HCVD method for mixed cation perovskite is promising for stable solar modules. Here the operational lifetime is measured with encapsulated 5 cm × 5 cm mini-modules with designated area of 22.4 cm^2. The module consists of 7 cells connected in series and exhibit designated area efficiency around 10%, which is consistent with a decay rate of 1.3%/decade (Figure S15 and 18). The operational lifetime was measured under a controlled temperature of 25 °C and continuous one-sun illumination with steady state power output. From Figure 5c we can first observe a burn-in loss of power output within approximately the first ten hours with 90% of its initial performance remaining.[40] A slow decay of the performance with a slope of -0.04%/h follows the burn-in loss, which corresponds to a T_{80} lifetime of 500 h.[41] These results demonstrate the good long-term stability of the $Cs_{0.1}FA_{0.9}PbI_{2.9}Br_{0.1}$ based solar module through our HCVD method.

Conclusions

In summary, with the mix-cation Cs/FA based perovskite films deposited by HCVD, the SnO_2/C_{60} ETL deposited by sputtering and thermal evaporation, and the Parylene encapsulation layer deposited by chemical vapor deposition, fully scalable perovskite solar modules with 91.8 cm^2 designated area on 100 cm^2 substrates are developed. Based on the fully vapor deposition process there is no limitation for the module area and the absolute efficiency decay is consistent with other commercialized photovoltaic techniques when scaling-up. The operational T_{80} lifetime under illumination is extrapolated approximately 500 h. With further interface engineering and perovskite film post treatment, the device performance is promising for improvement. We believe that HCVD will be a strong tool for perovskite photovoltaic towards commercialization.

Experimental

HCVD: The HCVD process is performed in a multi-zone tube furnace with solid FAI power as the precursor. The FAI power is first converted to the gas phase in the upstream zone when heated up to 190 °C. With the assistance of a low flux of carrier gas (air with a relative humidity of 45% in this case; flux = 60 sccm), the gas phase FAI is driven uniformly towards the downstream zone where the chemical reaction takes place between FAI and the pre-deposited $CsBr/PbI_2$ substrate. The

other end of tube furnace is connected to a pump, which results in an overall average vacuum level of approximately 1 torr in the furnace. The temperature of the downstream zone is approximately 150 °C. The pressure at the end with the input carrier gas is expected to be slightly higher and gradually decrease towards the end connected to the pump. The gentle gradient of pressure along the tube serves as the driving force to move FAI vapor from one end to the other. During HCVD, the FAI powder source is abundant, therefore to the first order approximation we can consider the FAI concentration in the gas stream to be a constant along the tube, if we do not take into account the slight decrease of the FAI concentration down the stream due to a small amount of FAI reacting with the $CsBr/PbI_2$ substrates. According to the equation $D_g \propto T^{3/2}/P$ (where D_g is the diffusion constant, T is the temperature, and P is the pressure),[9b] the diffusion rate of gas phase FAI to the substrate is approximately a constant. Also, the adsorption rate of FAI on the substrate can be assumed to be a constant independent (or only has a weak dependence) of the deposited film thickness. As a result, the film thickness of the deposited FAI is determined by the total deposition time and will be uniform across the entire length of the tube furnace.

Solar cell/module fabrication: Patterned FTO glass with sheet resistance around 7 Ω/□ (OPVT) was first ultrasonic washed sequentially with 1 wt% sodium dodecyl sulfate aqueous, de-ionized water, acetone and isopropanol for 15 min. The dry FTO substrate was then sputtered coated with 17 nm SnO_2 and evaporated with 5 nm C_{60}, with deposition rate of 0.7 nm/min and 0.02 nm/s, respectively. The perovskite active layer was deposited by HCVD developed in our early work,[8-9] with different precursor composition. PbI_2 and CsBr were thermally co-evaporated on C_{60} coated FTO/SnO_2 substrate with a rate of 0.10 nm/s and 0.01 nm/s, respectively, for 185 nm. The PbI_2/CsBr coated substrate was then transferred to a multi-zone tube furnace. The Cs salt is sensitive to water. To avoid the moisture effect, the tube furnace was quickly pumped down to 1 torr after loading the $CsBr/PbI_2$ substrate. The FAI vapor was carried by air with a humidity of 45%. The mixed O_2/N_2 carrier gas helps passivate shallow and deep traps in the converted perovskite film.[42] On the other hand, with such a low pressure level of air (1 torr) and the substrate temperature at approximately 150 °C, we expect the moisture in the carrier gas to have a minimal negative impact on the final perovskite film.[43] After reaction and cooling the perovskite film was washed with saturated potassium iodide solution (isopropanol) and annealed under 100 °C for 20 min. A hole transport material solution containing 29 mg spiro-MeOTAD, 11.5 µL TBP, and 7 µL Li-TFSI solution (520 mg/mL in acetonitrile) in 0.4 mL chlorobenzene was spin coated on top of the perovskite layer. For solar module the P2 patterning was performed by a CO_2 laser with a power of 5.6 W. At the end, 120 nm Au was thermally evaporated as back contact electrode and separated each sub-cell by mechanical scribing to form P3 patterning. The solar modules were encapsulated by 2 µm thick chemical vapor deposited Parylene and sealed by a cover glass with a thickness of 2 mm. This Parylene film was reported to be resistant to water.[37]

Characterization: The absorbance spectra of perovskite were recorded with a UV-vis spectrometer (Jasco V-670). The ultraviolet photoemission spectroscopy (UPS) and X-ray photoelectron spectroscopy (XPS) spectra were recorded from XPS-AXIS Ultra HAS (Kratos) equipped with monochromatic Al-Kα=1486.6 eV and non-monochromatic He-I=21.22 eV sources. Sample damage induced by UV and X-ray was monitored by taking five consecutive scans. Surface morphology and cross-section characterization were performed using a scanning electron microscope (FEI Quanta 250 FEG). Crystal structure of perovskite was measured by an X-ray Diffractometer (XRD) (Bruker D8 Discover). Time resolved photoluminescence (TRPL) of perovskite film on bare glass was acquired using the time-correlated, single-photon counting technique (Hamamatsu, C10627), and excitation was provided by a femtosecond mode-locked Ti:sapphire laser (SpectraPhysics, MAITAI XF-IMW) at 450 nm. J-V curves of solar cells/modules were recorded by a Keithley 2420 Source Meter. The simulated AM1.5 solar light comes from a solar simulator (Oriel-Sol1A equipped with a 450 W Xe lamp and an AM1.5 filter), with an illumination intensity of 100 mW/cm^2 calibrated by a reference Si solar cell. The designated area of 0.09 cm^2 for small cells, 22.4 cm^2 for small modules and 91.8 cm^2 for large modules were defined by corresponding metal mask. For solar cells/modules characterization, the dwell time is 10 ms, with small cell in the range of -0.1 V to 1.2 V, 5 cm × 5 cm modules in the range of -0.1 V to 7.0 V and 10 cm × 10 cm modules in the range of -1 V to 14.0 V. The EQE spectra of small cells were characterized by Oriel IQE 200.

Conflicts of interest

There are no conflicts to declare.

Acknowledgements

This work was supported by funding from the Energy Materials and Surface Sciences Unit of the Okinawa Institute of Science and Technology Graduate University, the OIST Proof of Concept (POC) Program, the OIST R&D Cluster Research Program, and JSPS KAKENHI Grant Number JP18K05266. We would like to thank OIST Mech. Eng. & Microfabrication Support Section for maintenance of cleanroom and sputtering equipment.

Notes and references

1 M. A. Green, Y. Hishikawa, E. D. Dunlop, D. H. Levi, J. Hohl-Ebinger, M. Yoshita, A. W. Y. Ho-Baillie, *Prog. Photovolt. Res. Appl*. **2019**, *27*, 3.
2 L. Qiu, L. K. Ono, Y. B. Qi, *Mater. Today Energy* **2018**, *7*, 169.
3 Z. Li, T. R. Klein, D. H. Kim, M. Yang, J. J. Berry, M. F. A. M. van Hest, K. Zhu, *Nat. Rev. Mater.* **2018**, *3*, 18017.
4 W. S. Yang, B.-W. Park, E. H. Jung, N. J. Jeon, Y. C. Kim, D. U. Lee, S. S. Shin, J. Seo, E. K. Kim, J. H. Noh, S. I. Seok, *Science* **2017**, *356*, 1376.

5 H. Chen, F. Ye, W. Tang, J. He, M. Yin, Y. Wang, F. Xie, E. Bi, X. Yang, M. Grätzel, L. Han, *Nature* **2017**, *550*, 92.

6 C. Longhua, L. Lusheng, W. Jifeng, D. Bin, G. Lili, F. Bin, *J. Semiconduc.* **2017**, *38*, 014006.

7 (a) L. K. Ono, M. R. Leyden, S. Wang, Y. B. Qi, *J. Mater. Chem. A* **2016**, *4*, 6693; (b) O. Malinkiewicz, A. Yella, Y. H. Lee, G. M. Espallargas, M. Graetzel, M. K. Nazeeruddin, H. J. Bolink, *Nat. Photon.* **2014**, *8*, 128; (c) D. Perez-del-Rey, P. P. Boix, M. Sessolo, A. Hadipour, H. J. Bolink, *J. Phys. Chem. Lett.* **2018**, *9*, 1041; (d) S. Wang, X. Li, J. Wu, W. Wen, Y. B. Qi, *Curr. Opin. Electrochem.* **2018**, *11*, 130.

8 M. R. Leyden, Y. Jiang, Y. B. Qi, *J. Mater. Chem. A* **2016**, *4*, 13125.

9 (a) M. R. Leyden, M. V. Lee, S. R. Raga, Y. B. Qi, *J. Mater. Chem. A* **2015**, *3*, 16097; (b) M. R. Leyden, L. K. Ono, S. R. Raga, Y. Kato, S. Wang, Y. B. Qi, *J. Mater. Chem. A* **2014**, *2*, 18742; (c) M. R. Leyden, L. Meng, Y. Jiang, L. K. Ono, L. Qiu, E. J. Juarez-Perez, C. Qin, C. Adachi, Y. B. Qi, *J. Phys. Chem. Lett.* **2017**, *8*, 3193.

10 M. Stolterfoht, C. M. Wolff, J. A. Márquez, S. Zhang, C. J. Hages, D. Rothhardt, S. Albrecht, P. L. Burn, P. Meredith, T. Unold, D. Neher, *Nat. Energy* **2018**, *3*, 847.

11 Y. Galagan, E. W. C. Coenen, W. J. H. Verhees, R. Andriessen, *J. Mater. Chem. A* **2016**, *4*, 5700.

12 D. H. Kim, J. B. Whitaker, Z. Li, M. F. A. M. van Hest, K. Zhu, *Joule* **2018**, *2*, 1437.

13 A. L. Palma, F. Matteocci, A. Agresti, S. Pescetelli, E. Calabrò, L. Vesce, S. Christiansen, M. Schmidt, A. D. Carlo, *IEEE J. Photovolt.* **2017**, *7*, 1674.

14 Y. Deng, X. Zheng, Y. Bai, Q. Wang, J. Zhao, J. Huang, *Nat. Energy* **2018**, *3*, 560.

15 M. Yang, Z. Li, M. O. Reese, O. G. Reid, D. H. Kim, S. Siol, T. R. Klein, Y. Yan, J. J. Berry, M. F. A. M. van Hest, K. Zhu, *Nat. Energy* **2017**, *2*, 17038.

16 M. Yang, D. H. Kim, T. R. Klein, Z. Li, M. O. Reese, B. J. Tremolet de Villers, J. J. Berry, M. F. A. M. van Hest, K. Zhu, *ACS Energy Lett.* **2018**, *3*, 322.

17 F. Di Giacomo, S. Shanmugam, H. Fledderus, B. J. Bruijnaers, W. J. H. Verhees, M. S. Dorenkamper, S. C. Veenstra, W. Qiu, R. Gehlhaar, T. Merckx, T. Aernouts, R. Andriessen, Y. Galagan, *Sol. Energy Mater. Sol. Cells* **2018**, *181*, 53.

18 (a) S. Wang, Y. Jiang, Emilio J. Juarez-Perez, Luis K. Ono, Y. B. Qi, *Nat. Energy* **2016**, *2*, 16195; (b) S.-H. Turren-Cruz, A. Hagfeldt, M. Saliba, *Science* **2018**, *362*, 449; (c) E. J. Juarez-Perez, Z. Hawash, S. R. Raga, L. K. Ono, Y. B. Qi, *Energy Environ. Sci.* **2016**, *9*, 3406; (d) E. J. Juarez-Perez, L. K. Ono, M. Maeda, Y. Jiang, Z. Hawash, Y. B. Qi, *J. Mater. Chem. A* **2018**, *6*, 9604.

19 M. Saliba, T. Matsui, J.-Y. Seo, K. Domanski, J.-P. Correa-Baena, M. K. Nazeeruddin, S. M. Zakeeruddin, W. Tress, A. Abate, A. Hagfeldt, M. Grätzel, *Energy Environ. Sci.* **2016**, *9*, 1989.

20 C. Yi, J. Luo, S. Meloni, A. Boziki, N. Ashari-Astani, C. Grätzel, S. M. Zakeeruddin, U. Röthlisberger, M. Grätzel, *Energy Environ. Sci.* **2016**, *9*, 656.

21 W. Rehman, D. P. McMeekin, J. B. Patel, R. L. Milot, M. B. Johnston, H. J. Snaith, L. M. Herz, *Energy Environ. Sci.* **2017**, *10*, 361.

22 Z. Yang, S. Zhang, L. Li, W. Chen, *J. Mater.* **2017**, *3*, 231.

23 Y. Jiang, M. R. Leyden, L. Qiu, S. Wang, L. K. Ono, Z. Wu, E. J. Juarez-Perez, Y. B. Qi, *Adv. Funct. Mater.* **2018**, *28*, 1703835.

24 L. Luo, Y. Zhang, N. Chai, X. Deng, J. Zhong, F. Huang, Y. Peng, Y.-B. Cheng, Z. Ku, *J. Mater. Chem. A* **2018**, *6*, 21143.

25 H.-S. Yoo, N.-G. Park, *Sol. Energy Mater. Sol. Cells* **2018**, *179*, 57.

26 G. Tong, H. Li, G. Li, T. Zhang, C. Li, L. Yu, J. Xu, Y. Jiang, Y. Shi, K. Chen, *Nano Energy*, **2018**, *48*, 536.

27 C. C. Stoumpos, C. D. Malliakas, M. G. Kanatzidis, *Inorg. Chem.* **2013**, *52*, 9019.

28 J. Endres, M. Kulbak, L. Zhan, B. P. Rand, D. Cahen, G. Hodes, A. Kahn, *J. Appl. Phys.* **2017**, *121*, 035304.

29 W. Tress, *Adv. Energy Mater.* **2017**, *7*, 1602358.

30 Z. Liu, L. Qiu, E. J. Juarez-Perez, Z. Hawash, T. Kim, Y. Jiang, Z. Wu, S. R. Raga, L. K. Ono, S. Liu, Y. B. Qi, *Nat. Commun.* **2018**, *9*, 3880.

31 L. Qiu, Z. Liu, L. K. Ono, Y. Jiang, D.-Y. Son, Z. Hawash, S. He, Y. B. Qi, *Adv. Funct. Mater.* **2018**, 1806779, DOI: 10.1002/adfm.201806779.

32 M. Batzill, K. Katsiev, J. M. Burst, U. Diebold, A. M. Chaka, B. Delley, *Phys. Rev. B* **2005**, *72*, 165414.

33 D. Yang, R. Yang, K. Wang, C. Wu, X. Zhu, J. Feng, X. Ren, G. Fang, S. Priya, S. Liu, *Nat. Commun.* **2018**, *9*, 3239.

34 (a) V. Sivaram, E. J. W. Crossland, T. Leijtens, N. K. Noel, J. Alexander-Webber, P. Docampo, H. J. Snaith, *J. Phys. Chem. C* **2014**, *118*, 1821; (b) M. Saliba, J.-P. Correa-Baena, C. M. Wolff, M. Stolterfoht, N. Phung, S. Albrecht, D. Neher, A. Abate, *Chem. Mater.* **2018**, *30*, 4193.

35 C. Xiao, C. Wang, W. Ke, B. P. Gorman, J. Ye, C.-S. Jiang, Y. Yan, M. M. Al-Jassim, *ACS. Appl. Mater. Inter.* **2017**, *9*, 38373.

36 J. P. Bastos, E. Voroshazi, E. Fron, G. Brammertz, T. Vangerven, M. V. Auweraer, J. Poortmans, D. Cheyns, *ACS Appl. Mater. Interfaces* **2016**, *8*, 9798.

37 H. Jinno, K. Fukuda, X. Xu, S. Park, Y. Suzuki, M. Koizumi, T. Yokota, I. Osaka, K. Takimiya, T. Someya, *Nat. Energy* **2017**, *2*, 780.

38 F. Matteocci, L. Cinà, F. Di Giacomo, S. Razza, A. L. Palma, A. Guidobaldi, A. D'Epifanio, S. Licoccia, T. M. Brown, A. Reale, A. Di Carlo, *Prog. Photovolt. Res. Appl.* **2016**, *24*, 436.

39 Z. Tang, T. Bessho, F. Awai, T. Kinoshita, M. M. Maitani, R. Jono, T. N. Murakami, H. Wang, T. Kubo, S. Uchida, H. Segawa, *Sci. Rep.* **2017**, *7*, 12183.

40 J. A. Christians, P. Schulz, J. S. Tinkham, T. H. Schloemer, S. P. Harvey, B. J. Tremolet de Villers, A. Sellinger, J. J. Berry, J. M. Luther, *Nat. Energy* **2018**, *3*, 68.

41 K. Domanski, E. A. Alharbi, A. Hagfeldt, M. Grätzel, W. Tress, *Nat. Energy* **2018**, *3*, 61.

42 A. Ng, Z. Ren, Q. Shen, S. H. Cheung, H. C. Gokkaya, S. K. So, A. B. Djurišić, Y. Wan, X. Wu, C. Surya, *ACS Appl. Mater. Interfaces*, **2016**, *8*, 32805.

43 J. Huang, S. Tan, P. D. Lund, H. Zhou, *Energy Environ. Sci.*, **2017**, *10*, 2284.